

**A comparison of global heat flow interpolation
techniques**

Buchanan C. Kerswell¹Matthew J. Kohn¹

¹Department of Geosciences, Boise State University, Boise, ID 83725

Key Points:

-
-
-

9 **Abstract**

```

10      ## Loading libraries:
11      ## magrittr
12      ## ggplot2
13      ## tidyverse
14      ## readr
15      ## purrr
16      ## gstat
17      ## ggslab
18      ## sf
19      ## ggrepel
20      ## patchwork
21      ## cowplot
22      ## dplyr
23      ## Loading functions

```

24 **1 Introduction**

25 Heat escaping the solid Earth's surface indicates a dynamically cooling planet. Surface heat flow databases (Hasterok & Chapman, 2008; Luazeau, 2019; Pollack et al., 1993) provide a way to understand geodynamics by relating the amount of heat escaping Earth's surface to heat-transferring and heat-generating subsurface processes such as diffusion, hydrothermal circulation, radioactive decay, fault motion, subduction dynamics, and mantle convection (Currie et al., 2004; Currie & Hyndman, 2006; Fourier, 1827; Furlong & Chapman, 2013; Furukawa, 1993; Gao & Wang, 2014; Hasterok, 2013; Kerswell et al., 2020; Parsons & Sclater, 1977; Pollack & Chapman, 1977; Rudnick et al., 1998; Stein & Stein, 1992, 1994; Wada & Wang, 2009). Surface heat flow observations continue to motivate research, evident by more than 1,393 publications compiled in the most recent heat flow dataset, although the rate of publications using surface heat flow has declined since the mid 1980's (Jennings & Hasterok, 2021).

37 Many research questions, such as calculating the global surface heat flux from continents and oceans, require interpolating discrete heat flow observations onto a continuous approximation of Earth's surface. Previous attempts at interpolation use one or

more geographic, geologic, geochronologic, or geophysical proxies to predict heat flow at unknown locations by association with similar observation sites (e.g., bathymetry or elevation, proximity to active or ancient orogens, seafloor age, upper mantle shear wave velocities, Chapman & Pollack, 1975; Davies, 2013; Goutorbe et al., 2011; Lee & Uyeda, 1965; Lucaleau, 2019; Sclater & Francheteau, 1970; Shapiro & Ritzwoller, 2004). These methods are called *similarity methods* (Figure 1). The success of such interpolations are typically evaluated statistically by the misfit between the predicted and observed heat flow. However, even statistically-successful heat flow interpolations are difficult to interpret and show unexpected anomalies (Lucaleau, 2019). The fidelity and usefulness of interpolations depend on the question being asked and the choice of methodology.

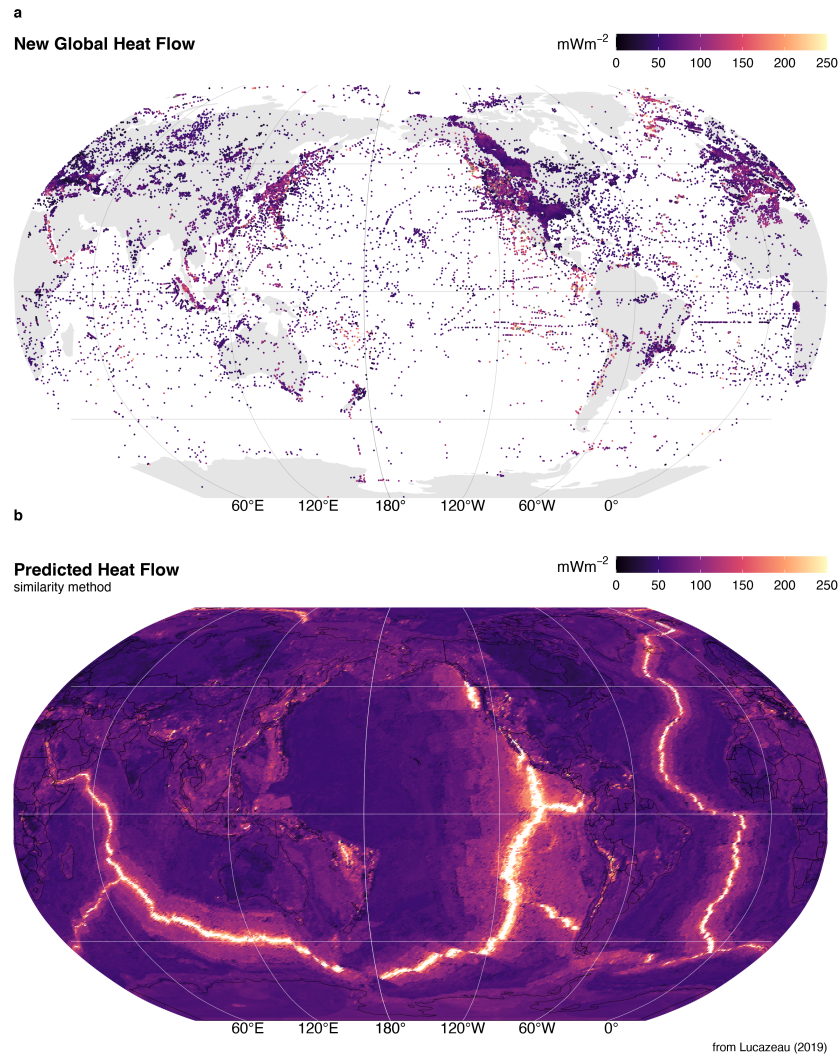


Figure 1: The NGHF dataset. (a) The complete dataset ($n = 69729$), and (b) interpolation by similarity method from Lucaleau (2019).

Predicting surface heat flow by association with physical proxies is arguably the most reasonable approach to interpolation for global investigations. Our understanding of geodynamics and near-surface heat flow perturbations implies that the variance in surface heat flow is not uniformly stochastic, but rather, in large part, determined by the physical conditions and processes operating locally (e.g., Goutorbe et al., 2011). For example, younger oceanic plates should have higher surface heat flow than older plates (Stein & Stein, 1992), subducting oceanic plates will lower surface heat flow near trenches (Furukawa, 1993), and hydrothermal circulation of seawater can modify heat flow in oceanic crust (Hasterok et al., 2011). Interpolation by association with physical proxies makes reasoned predictions of heat flow based on many independently-tested geodynamic models. However, similarity methods are strongly biased towards such models and risk making determinations where, in fact, surprising results and idiosyncrasies may be found.

In contrast, there exists some degree of stationarity, spatial dependence, or continuity, in the distribution of surface heat flow. A pair of surface heat flow observations taken one meter apart will be strongly correlated. The correlation between pairs of observations will likely decrease with increasing distance between the pairs (Goovaerts, 1997). The spatial (dis)continuity of surface heat flow represents the areal extent of geodynamic processes and their interactions. For example, consistent patterns of heat flow near volcanic arcs are interpreted to reflect common backarc lithospheric thermal structures and slab-mantle mechanical coupling depths in subduction zones (Furukawa, 1993; Kerswell et al., 2020; Wada & Wang, 2009).

In theory, one may predict surface heat flow at unknown locations by considering many nearby observations (i.e. Kriging, Krige, 1951). However, Kriging is disadvantageous for global interpolations of surface heat flow because it assumes that the underlying distribution of heat flow is stationary (constant in space), which effectively ignores geodynamic complexity. One can overcome this problem by relaxing assumptions of stationarity, or applying Markov-Bayes techniques to include proxies as priors (Bárdossy, 1997). Instead, we leverage the properties of stationarity as a tool for comparison with *similarity* methods of interpolation (Goutorbe et al., 2011; Lucaleau, 2019). So the questions are: 1) What are the differences between Kriging and similarity methods? 2) What are the implications of the differences according to the implicit assumptions in both methods?

We attempt to answer these questions by using ordinary Kriging to interpolate the New Global Heat Flow (NGHF) dataset of Lucaleau (2019). Our method is optimized using a genetic algorithm to minimize an objective function which considers both the misfit on the variogram models and interpolation results (after Li et al., 2018). We then compare our interpolation results to those of Lucaleau (2019) and consider the implications of Kriging vs. similarity methods of interpolation. We restrict our comparison to areas near subduction zone segments defined by Syracuse & Abers (2006) for two reasons: 1) to provide maps and statistics useful to subduction zone research, and 2) to emphasize differences and idiosyncrasies in both interpolation approaches in a complex tectonic and thermal setting.

2 Methods

2.1 The NGHF Dataset

The NGHF dataset was downloaded from the supplementary material of Lucaleau (2019). It contains 69729 data points, their locations in latitude/longitude, and metadata—including a data quality rank (Code 6) from A to D (with Code 6 = Z = undetermined). The reader is referred to Lucaleau (2019) for details on compilation, references, and historical perspective on the NGHF and previous compilations. We use NGHF because it is the most recent dataset available, has been carefully compiled, and is open-access.

Like Lucaleau (2019), we exclude 4790 poor quality observations (Code 6 = D) from our analysis. We further remove 350 data points without heat flow observations and two without geographic information. Multiple observations at the same location are parsed to avoid singular covariance matrices during Kriging:

$$\begin{aligned}
 f(X_i^q, Y_i^q) = \\
 X_i^q > Y_i^q \rightarrow z_i = x_i \\
 X_i^q < Y_i^q \rightarrow z_i = y_i \\
 X_i^q = Y_i^q \rightarrow z_i = RAND(x_i, y_i)
 \end{aligned} \tag{1}$$

where X_i^q and Y_i^q represent the quality of each duplicate observation pair at location i , $RAND$ is a random function that selects either the observation x_i or y_i , and z_i

106 stores the observation selected by $f(X_i^q, Y_i^q)$. The final dataset used for Kriging has $n =$
 107 55274 observations after parsing $n = 32430$ duplicate observation.

108 **2.2 Kriging**

109 Kriging is a three-step process that involves first estimating an experimental variogram,
 110 $\hat{\gamma}(h)$, fitting the experimental variogram with one of many variogram models,
 111 $\gamma(h)$, and finally using the modelled variogram to predict random variables at unknown
 112 locations (Cressie, 2015; Krige, 1951). We use the general-purpose functions defined in
 113 the “R” package **gstat** (Gräler et al., 2016; Pebesma, 2004) to perform all three steps.
 114 We begin by estimating an experimental variogram as defined by Bárdossy (1997):

$$\hat{\gamma}(h) = \frac{1}{2N(h)} \sum_{N(h)} (Z(u_i) - Z(u_j))^2 \quad (2)$$

115 where $N(h)$ is the number of pairs of points, $Z(u_i)$ and $Z(u_j)$, separated by a lag
 116 distance, $h = |u_i - u_j|$. We evaluate $\hat{\gamma}(h)$ at fifteen lag distances by binning the irregular
 117 spaced data with a bin width, δ , equal to one-third of the maximum lag distance
 118 divided by the number of lags used to evaluate the variogram, $\delta = \max(N(h))/(3 \cdot 15)$.
 119 Then $N(h) \leftarrow N(h, \delta h) = \{i, j : |u_i - u_j| \in [h - \delta h, h + \delta h]\}$. In simple terms, Equa-
 120 tion 2 represents the similarity, or dissimilarity, between pairs of observations in space.
 121 Equation 2 is derived from the theory of *regionalized variables* (Matheron, 1963, 2019),
 122 which formally defines a probabilistic framework for spatial interpolation of natural phe-
 123 nomena. It is important for the reader to understand the fundamental assumptions im-
 124 plicit in Equation 2 in order to understand the comparison of interpolation techniques
 125 discussed later. The basic assumptions used in our Kriging method are:

- 126 • $\hat{\gamma}(h)$ is directionally invariant (isotropic)
- 127 • $\hat{\gamma}(h)$ is evaluated in two-dimensions and neglects elevation, $Z(u) \in \mathbb{R}^2$
- 128 • The first and second moments of $Z(u)$ have the following conditions over the do-
 129 main D :

$$\begin{aligned} E[Z(u)] &= \text{mean} = \text{constant}, & \forall u \in D \\ E[(Z(u + h) - \text{mean})(Z(u) - \text{mean})] &= C(h), & \forall |u, u + h| \in D \end{aligned} \quad (3)$$

The last assumption (Equation 3) is called “second-order stationarity” and is commonly used in practice. It assumes the underlying probability distribution of the random variable, $Z(u)$, does not change in space and the covariance, $C(h)$, only depends on the distance, h , between two random variables. These assumptions are expected to be valid in cases where the underlying natural process is stochastic, spatially continuous, and has the property of additivity such that $\frac{1}{n} \sum_{i=1}^n Z(u_i)$ has the same meaning as $Z(u)$ (Bárdossy, 1997).

The following are two illustrative cases where Equation 3 is likely valid:

1. The thickness of a sedimentary unit with a homogeneous concentration of radioactive elements can be approximated by $q_s = q_b + \int A dz$, where q_b is a constant heat flux entering the bottom of the layer and A is the heat production within the layer with thickness z (Furlong & Chapman, 2013). If we have two samples, $Z(u_1) = 31 \text{ mW/m}^2$ and $Z(u_2) = 30.5 \text{ mW/m}^2$, their corresponding thicknesses would be $Z'(u_1) = 1000 \text{ m}$ and $Z'(u_2) = 500 \text{ m}$ for $A = 0.001 \text{ mW/m}^3$ and $q_b = 30 \text{ mW/m}^2$. The variable, $Z(u)$, in this case is additive because the arithmetic mean of the samples is a good approximation of the average sedimentary layer thickness, $(Z(u_1) + Z(u_2))/2 = 750 \text{ m}$.
2. The age of young oceanic lithosphere can be approximated by $q_s(t) = kT_b(\pi\kappa t)^{-1/2}$, where $q_s(t)$ is the surface heat flow of a plate with age, t , T_b is the temperature at the base of the plate, k is thermal conductivity, and $\kappa = k/\rho C_p$ is thermal diffusivity (Stein & Stein, 1992). For $k = 3.138 \text{ W/mK}$, $\rho = 3330 \text{ kg/m}^3$, $C_p = 1171 \text{ J/kgK}$, $T_b = 1350^\circ\text{C}$, two samples, $Z(u_1) = 180 \text{ mW/m}^2$ and $Z(u_2) = 190 \text{ mW/m}^2$, would correspond to plates with ages of $Z'(u_1) = 10 \text{ Ma}$, and $Z'(u_2) = 9 \text{ Ma}$, respectively. Since $Z(u_1)+Z(u_2)/2 = 185 \text{ mW/m}^2$ and $Z'(185 \text{ mW/m}^2) = 9.5 \text{ Ma} = Z'(u_1) + Z'(u_2)/2$, the variable $Z(u)$ in this case is also additive.

In contrast, Equation 3 is likely invalid in regions that transition among two or more tectonic regimes. For example, the expected heat flow $E[Z(u)] = \text{mean}$ will change when moving from a spreading center to a subduction zone. $E[Z(u)] = \text{mean} \neq \text{constant}$ over the region of interest. Proceeding with Equation 3 in this case has the effect of masking the geodynamic complexity. In other words, the spatial dependence is considered in the Kriging method in this case, but the geodynamic structure is *invisible*. We will see that this has important implications when comparing our Kriging method to Lucaleau

(2019)'s interpolation method, which is exactly opposite of this formalism—it only considers the similarities among physical proxies and not spatial dependence.

The second step is to fit the experimental variogram with a variogram model, $\gamma(h)$. In this study we fit two popular variogram models to the experimental variogram. We use models with sills, which implies the spatial dependence between pairs of points has a finite range. The spherical and exponential variogram models used in this study are defined as (Chiles & Delfiner, 2009; Cressie, 2015):

$$sph \leftarrow \gamma(h) = \begin{cases} n + s \left(\frac{3h}{2a} - \frac{1}{2} \left(\frac{h}{a} \right)^3 \right), & \text{if } 0 \leq h \leq a \\ n + s, & \text{if } h > a \end{cases} \quad (4)$$

$$exp \leftarrow \gamma(h) = n + s \left(1 - exp \left(\frac{-h}{a} \right) \right), \quad \text{if } h \geq 0$$

where n is the nugget, s is the sill, and a is the effective range. The effective range, a , is related to the range, r , by $a = r$ and $a = r/3$ for spherical and exponential models, respectively (Gräler et al., 2016; Pebesma, 2004). We use the function `fit.variogram` in `gstat` to try both variogram models. The best model is selected by the minimum misfit by weighted least square (WLS, Pebesma, 2004).

We use ordinary Kriging for our interpolation step, which predicts the value of a random function, $\hat{Z}(u)$, at unknown locations as a linear combination of all known locations in the domain, D (Bárdossy, 1997):

$$\hat{Z}(u) = \sum_{i=1}^n \lambda_i Z(u_i), \quad \forall u \in D \quad (5)$$

The conditions in Equation 3 set up a constrained minimization problem since one has:

$$E[Z(u)] = mean, \quad \forall u \in D \quad (6)$$

The linear estimator must obey

$$E[\hat{Z}(u)] = \sum_{i=1}^n \lambda_i E[Z(u_i)] = mean \quad (7)$$

180 so the weights must be:

$$\sum_{i=1}^n \lambda_i = 1 \quad (8)$$

181 This is the first constraint, also known as the unbiased condition, which states that
 182 the sum of the weights must equal one. However, there is an infinite set of real numbers
 183 one could use for the weights, λ_i . Our goal is to find the set of weights in Equation 5 that
 184 minimizes the estimation variance. This can be solved with the covariance function, $C(h)$
 185 from Equation 3:

$$\begin{aligned} \sigma^2(u) &= \text{Var}[Z(u) - \hat{Z}(u)] = E \left[(Z(u) - \sum_{i=1}^n \lambda_i Z(u_i))^2 \right] = \\ &= E \left[Z(u)^2 + \sum_{j=1}^n \sum_{i=1}^n \lambda_j \lambda_i Z(u_j) Z(u_i) - 2 \sum_{i=1}^n \lambda_i Z(u_i) Z(u) \right] = \\ &= C(0) + \sum_{j=1}^n \sum_{i=1}^n \lambda_j \lambda_i C(u_i - u_j) - 2 \sum_{i=1}^n \lambda_i C(u_i - u) \end{aligned} \quad (9)$$

186 Solving for the weights in Equation 5 with respect to the unbiased condition (Equation
 187 8) and minimum estimate variance (Equation 9), yields the best linear unbiased es-
 188 timator (BLUE, Bárdossy, 1997). In our case, this is done by the function `krige` in `gstat`.

189 2.3 Kriging Optimization

190 Achieving a useful Kriging results depends on one's choice of many Kriging param-
 191 eters (Θ). In this study, we investigate a set of parameters, Θ :

$$\Theta = \{c, w, m, s, a, n, S\} \quad (10)$$

192 where c is the lag cutoff proportion, w is the lag window, m is the model type (sph
 193 or exp), s is the sill, a is the effective range, n is the nugget, and S is the maximum dis-
 194 tance for local Kriging. Only points within S from the prediction location are used for
 195 Kriging. The lag cutoff is the maximum separation distance between pairs of points used
 196 in the experimental variogram (i.e. the x-axis maximum limit) calculated as a fraction
 197 of the overall maximum separation distance for all observations, $Z(u)$, in the domain,
 198 D . The lag window, w , shifts the lags where the variogram is evaluated by removing the

199 first n lags and adding n lags to the right side of the variogram. This is necessary to avoid
 200 negative ranges, a , when fitting experimental variograms with anomalously high vari-
 201 ances at small lag distances.

202 Our goal is to find Θ such that our interpolation, $f(x_i; \Theta)$, gives the most useful
 203 outcome—defined by minimizing a cost function, $C(\Theta)$, that represents the error between
 204 the set of real observations, $Z(u_i)$ and predictions, $\hat{Z}(u)$. We define a cost function that
 205 simultaneously considers the misfit between the experimental and modelled variogram
 206 and between the Kriging predictions and observed heat flow (after Li et al., 2018):

$$C(\Theta) = (1 - w)C_F(\Theta) + wC_I(\Theta) \quad (11)$$

207 where $C_F(\Theta)$ is the root mean square error (RMSE) of the modelled variogram fit
 208 calculated by WLS, and $C_I(\Theta)$ is the RMSE of the Kriging result calculated by cross-
 209 validation. The weight, w , is set to 0.5 in our study, which balances the effects of $C_F(\Theta)$
 210 and $C_I(\Theta)$ on the cost function. The final expression to minimize becomes:

$$\min(C(\Theta)) = \frac{1-w}{\sigma_E} \sqrt{\frac{1}{N} \sum_{k=1}^N w(h_k)[\hat{\gamma}(h_k) - \gamma(h_k; \Theta)]^2} + \frac{w}{\sigma_S} \sqrt{\frac{1}{M} \sum_{i=1}^M [Z(u_i) - \hat{Z}(u_i; \Theta)]^2} \quad (12)$$

211 where N is the number of pairs of points used to calculate the experimental var-
 212 iogram, $\hat{\gamma}(h_k)$, σ_E is the standard deviation of the experimental variogram, $\hat{\gamma}(h)$, $w(h_k)$
 213 is the weight in WLS and defines the importance of the k th lag in the error estimate.
 214 We use $w(h_k) = N_k/h_k^2$. $Z(u_i)$ and $\hat{Z}(u_i; \Theta)$ are the measured and predicted values,
 215 respectively, σ_S is the standard deviation of the predicted values, $\hat{Z}(u_i)$, and M is the
 216 number of measurements in $Z(u_i)$. For $C_I(\Theta)$ we use ten-fold cross-validation, which splits
 217 the dataset, $|Z(u_i), \forall u_i \in D|$ into ten equal intervals and tests one interval against the
 218 remaining nine. This process is then repeated over all intervals so that the whole dataset
 219 has been cross-validated.

220 Minimization of $C(\Theta)$ is achieved by a genetic algorithm that simulates biologic
 221 natural selection by differential success (Goldberg, 1989). Our procedure is as follows:

- 222 1. Initiate fifty *chromosomes*, ξ , with random starting parameters defined within the
 223 search domain (Table 1)
- 224 2. Evaluate the fitness of each individual chromosome as $-C(\Theta)$ for the entire pop-
 225 ulation
- 226 3. Allow the population to exchange genetic information by sequentially performing
 227 genetic operations:
- 228 a. Selection: the top 5% fittest chromosomes survive each generation
- 229 b. Crossover: pairs of chromosomes have an 80% chance of exchanging genetic in-
 230 formation
- 231 c. Mutation: there is a 10% chance for random genetic mutations
- 232 4. Evaluate the fitness of the new population
- 233 5. If the termination criterion is met, do step (6), otherwise continue to evolve by
 234 repeating steps (3) and (4)
- 235 6. Decode the best chromosome and build the optimal variogram

236 We use the general-purpose functions in the “R” package **GA** (Scrucca, 2013, 2016)
 237 to perform each step in the above procedure.

Table 1: Parameters and ranges used in the optimization algorithm

Parameter	Search Domain	Units
Lag Cutoff (c)	[1/3, 1/15]	NA
Lag Window (w)	[1, 5]	NA
Model (m)	[Spherical, Exponential]	NA
Sill (s)	[1, $1000\sqrt{2}$]	mWm^{-2}
Effective Range (a)	[1, 1×10^3]	km
Nugget (n)	[1, $1000\sqrt{2}$]	mWm^{-2}
Local Search (S)	[1, 1×10^3]	km

238 2.4 Map Projection and Interpolation Grid

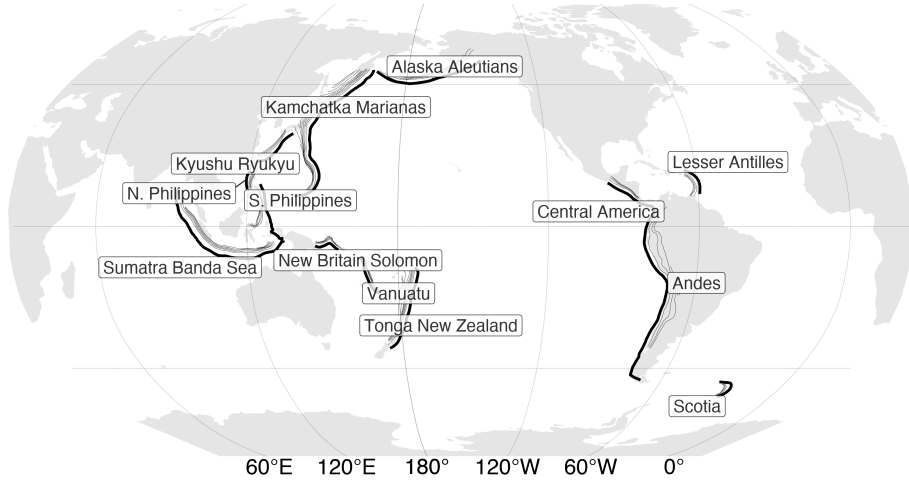
239 We interpolate onto the same $0.5^\circ\text{C} \times 0.5^\circ\text{C}$ grid as Lucaleau (2019) so a direct
 240 difference could be calculated between our interpolation methods and Lucaleau (2019)’s.

241 The NGHF and grid with predicted heat flow from Lucaleau (2019) were transformed
242 into a Pacific-centered Robinson coordinate reference system (CRS) defined using the
243 proj string (PROJ contributors, 2021):

244 `+proj=robin +lon_0=-155 +lon_wrap=-155 +x_0=0 +y_0=0`
245 `+ellps=WGS84 +datum=WGS84 +units=m +no_defs`

246 All geographic operations, including Kriging, are performed in the above CRS us-
247 ing the general-purpose functions in the “R” package **sf** (Pebesma, 2018). We define the
248 Kriging domain near individual arc segments in two steps: 1) 1000 *km* buffers are drawn
249 around the arc segments as defined by Syracuse & Abers (2006). 2) The bounding box
250 of the 1000 *km* buffer is expanded by 10% on all sides (Figure 2). We provide the com-
251 plete NGHF dataset (Lucaleau, 2019), filtered and parsed NGHF dataset, heat flow in-
252 terpolations (from Lucaleau, 2019, and this study), and our code as supplementary in-
253 formation to support FAIR data policy (Wilkinson et al., 2016). These items can also
254 be retrieved from the official repository at <https://doi.org/10.17605/OSF.IO/CA6ZU>.

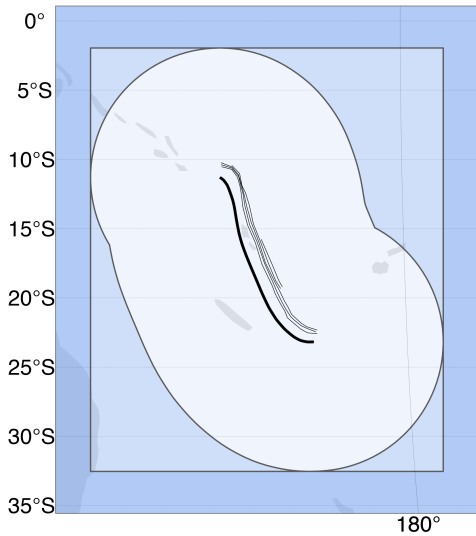
a Subduction Zone Segments



from Syracuse & Abers (2006)

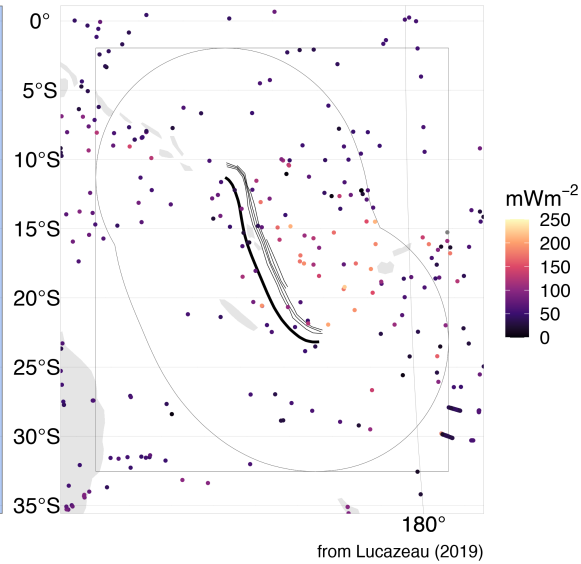
b Vanuatu

Interpolation Domain



c Vanuatu

n = 349



from Lucazeau (2019)

Figure 2: Subduction zone segments and interpolation domain. (a) Heat flow is interpolated around thirteen subduction zone segments by (b) drawing a 1000km buffer (lightest blue) around each segment and expanding the buffer's bounding box (medium blue) by 10% on all sides (darkest blue). (c) The NGHF dataset is cropped within the largest rectangle. Data from Syracuse & Abers (2006) and Lucazeau (2019).

255 **3 Results**256 **3.1 Heat Flow Near Subduction Zone Segments**

257 Summary statistics for surface heat flow observations by subduction zone segment
 258 are given in Table 2 and Figure 3. Surface heat flow is centered around $45\text{-}70 \text{ mW m}^{-2}$
 259 (medians) and narrowly distributed with inter-quartile ranges (IQR) from 12 to 50 mW m^{-2}
 260 for most subduction zone segments, excluding outliers. Alaska Aleutians is the excep-
 261 tion with a broad (IQR = 250 mW^{-2}) range of heat flow with a median of 184 mW m^{-2} .
 262 The whole distribution, including outliers, for all segments are strongly right-skewed with
 263 maximum heat flow values of several thousand of mW m^{-2} or more. Heat flow values
 264 above 250 mW m^{-2} are considered geothermal areas by Lucaleau (2019), which we adopt
 265 as a relevant empirical limit for anomalously high heat flow.

Table 2: Heat flow (mW m^{-2}) observations by subduction zone segment

Segment	n	Min	Max	Median	IQR	Mean	Sigma
Alaska Aleutians	2792	4	7765	184	206	233	344
Andes	5226	7	911	45	50	87	88
Central America	5038	8	911	45	48	88	91
Kamchatka Marianas	3956	1	31000	71	48	121	658
Kyushu Ryukyu	3246	1	31000	72	44	130	726
Lesser Antilles	3534	13	1150	41	12	52	50
N. Philippines	1001	3	31000	72	35	206	1276
New Britain Solomon	181	3	174	65	42	69	30
S. Philippines	1442	1	31000	71	43	167	1063
Scotia	72	13	145	76	23	74	28
Sumatra Banda Sea	3037	1	5600	65	47	77	120
Tonga New Zealand	507	1	416	54	40	64	45
Vanuatu	349	1	283	54	40	64	44

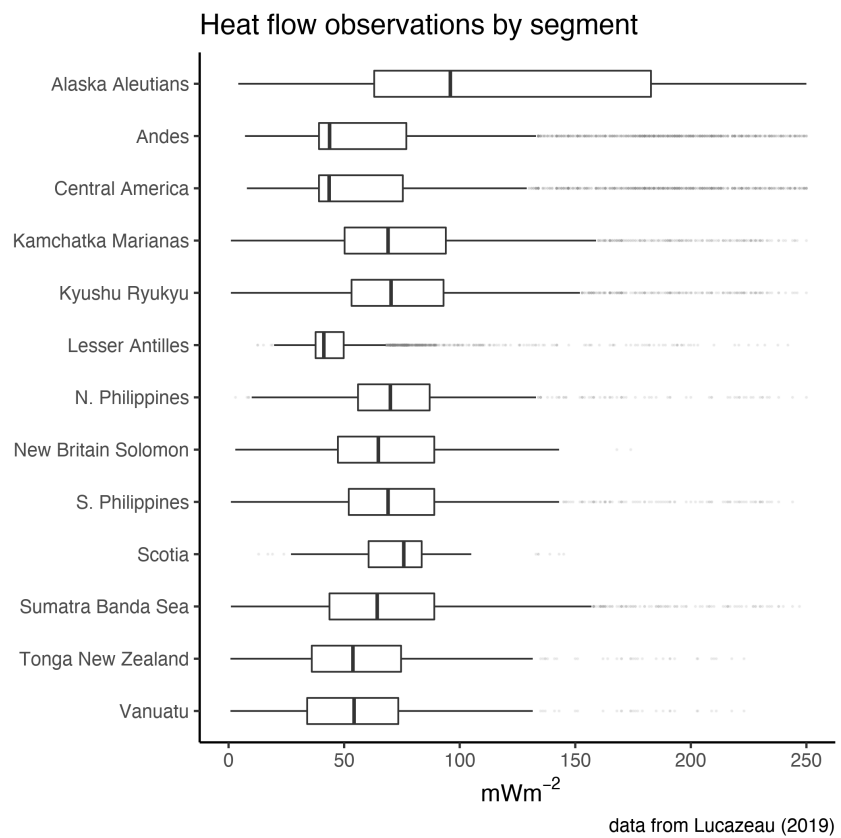


Figure 3: Distribution of heat flow observations by subduction zone segment. Heat flow near most segments are centered around 50 mW m^{-2} and highly skewed right. The skewness likely represents sampling near hydrothermal systems, volcanic arcs, or spreading centers. Data from Luazeau (2019)

266 The optimal variogram models and associated errors $C_F(\Theta)$ and $C_I(\Theta)$ are given
 267 in Table 3.

Table 3: Optimal varigram models by subduction zone segment

Segment	Model	Sill [mWm^{-2}]	Range [km]
Alaska Aleutians	Sph	284	219
Andes	Sph	87	344
Central America	Sph	86	342
Kamchatka Marianas	Exp	692	274
Kyushu Ryukyu	Sph	911	1676
Lesser Antilles	Exp	37	98
N. Philippines	Sph	1358	243
New Britain Solomon	Exp	28	76
S. Philippines	Sph	1163	421
Scotia	Exp	9	4
Sumatra Banda Sea	Exp	113	32
Tonga New Zealand	Sph	47	131
Vanuatu	Sph	48	574

268 Summary statistics for the interpolation differences are given in Table 4 and Fig-
 269 ure ??.

Table 4: Predicted heat flow (mWm^{-2}) differences by subduction zone segment

Segment	Min	Max	Median	IQR	Mean	Sigma
Alaska Aleutians	-550	2690	-2	20	3	71
Andes	-188	2336	2	35	13	72
Central America	-189	2731	8	62	44	146
Kamchatka Marianas	-2777	297	4	15	4	45
Kyushu Ryukyu	-2781	168	5	24	2	85
Lesser Antilles	-103	572	0	16	6	31
N. Philippines	-2800	278	0	26	-5	94
New Britain Solomon	-81	240	1	22	5	20
S. Philippines	-274	375	5	26	7	29
Scotia	-62	1001	-4	24	5	33
Sumatra Banda Sea	-243	385	-2	20	1	19
Tonga New Zealand	-113	1695	-9	23	-2	30
Vanuatu	-166	1657	7	27	8	40

270 **4 Discussion**271 **5 Conclusions**272 **Acknowledgments**

273 **References**

- 274 Bárdossy, A. (1997). Introduction to geostatistics. *Institute of Hydraulic Engineering,*
 275 *University of Stuttgart.*
- 276 Chapman, D. S., & Pollack, H. N. (1975). Global heat flow: A new look. *Earth and Plan-*
 277 *etary Science Letters, 28*(1), 23–32.
- 278 Chiles, J.-P., & Delfiner, P. (2009). *Geostatistics: Modeling spatial uncertainty* (Vol. 497).
 279 John Wiley & Sons.
- 280 Cressie, N. (2015). *Statistics for spatial data*. John Wiley & Sons.
- 281 Currie, C., & Hyndman, R. D. (2006). The thermal structure of subduction zone back
 282 arcs. *Journal of Geophysical Research: Solid Earth, 111*(B8).
- 283 Currie, C., Wang, K., Hyndman, R. D., & He, J. (2004). The thermal effects of steady-
 284 state slab-driven mantle flow above a subducting plate: The Cascadia subduction zone
 285 and backarc. *Earth and Planetary Science Letters, 223*(1-2), 35–48.
- 286 Davies, J. H. (2013). Global map of solid earth surface heat flow. *Geochemistry, Geo-*
 287 *physics, Geosystems, 14*(10), 4608–4622.
- 288 Fourier, J. (1827). Mémoire sur les températures du globe terrestre et des espaces planétaires.
 289 *Mémoires de l'Académie Royale Des Sciences de l'Institut de France, 7*, 570–604.
- 290 Furlong, K. P., & Chapman, D. S. (2013). Heat flow, heat generation, and the thermal
 291 state of the lithosphere. *Annual Review of Earth and Planetary Sciences, 41*, 385–
 292 410.
- 293 Furukawa, Y. (1993). Depth of the decoupling plate interface and thermal structure un-
 294 der arcs. *Journal of Geophysical Research: Solid Earth, 98*(B11), 20005–20013.
- 295 Gao, X., & Wang, K. (2014). Strength of stick-slip and creeping subduction megathrusts
 296 from heat flow observations. *Science, 345*(6200), 1038–1041.
- 297 Goldberg, D. E. (1989). Genetic algorithms in search. *Optimization, and MachineLearn-*
 298 *ing.*
- 299 Goovaerts, P. (1997). *Geostatistics for natural resources evaluation*. Oxford University
 300 Press on Demand.

- 301 Goutorbe, B., Poort, J., Lucaleau, F., & Raillard, S. (2011). Global heat flow trends re-
302 solved from multiple geological and geophysical proxies. *Geophysical Journal International*, 187(3), 1405–1419.
- 303
- 304 Gräler, B., Pebesma, E., & Heuvelink, G. (2016). Spatio-temporal interpolation using
305 gstat. *The R Journal*, 8, 204–218. Retrieved from <https://journal.r-project.org/archive/2016/RJ-2016-014/index.html>
- 306
- 307 Hasterok, D. (2013). A heat flow based cooling model for tectonic plates. *Earth and Plan-
308 etary Science Letters*, 361, 34–43.
- 309
- 310 Hasterok, D., & Chapman, D. (2008). Global heat flow: A new database and a new ap-
proach. In *AGU fall meeting abstracts* (Vol. 2008, pp. T21C–1985).
- 311
- 312 Hasterok, D., Chapman, D., & Davis, E. (2011). Oceanic heat flow: Implications for global
heat loss. *Earth and Planetary Science Letters*, 311(3-4), 386–395.
- 313
- 314 Jennings, S., & Hasterok, D. (2021). HeatFlow.org. *Heatflow.org*. Retrieved from <http://heatflow.org/>
- 315
- 316 Kerswell, B. C., Kohn, M. J., & Gerya, T. V. (2020). Backarc lithospheric thickness and
317 serpentine stability control slab-mantle coupling depths in subduction zones. *Earth
and Space Science Open Archive*, 34. [https://doi.org/10.1002/essoar.10503710
.1](https://doi.org/10.1002/essoar.10503710.1)
- 318
- 319 Krige, D. G. (1951). A statistical approach to some basic mine valuation problems on
320 the witwatersrand. *Journal of the Southern African Institute of Mining and Metal-
321 lurgy*, 52(6), 119–139.
- 322
- 323 Lee, W. H., & Uyeda, S. (1965). Review of heat flow data. *Terrestrial Heat Flow*, 8, 87–
190.
- 324
- 325 Li, Z., Zhang, X., Clarke, K. C., Liu, G., & Zhu, R. (2018). An automatic variogram mod-
eling method with high reliability fitness and estimates. *Computers & Geosciences*,
326 120, 48–59.
- 327
- 328 Lucazeau, F. (2019). Analysis and mapping of an updated terrestrial heat flow data set.
Geochemistry, Geophysics, Geosystems, 20(8), 4001–4024.
- 329 Matheron, G. (1963). Principles of geostatistics. *Economic Geology*, 58(8), 1246–1266.

- 330 Matheron, G. (2019). *Matheron's theory of regionalized variables*. International Asso-
331 ciation for.
- 332 Parsons, B., & Sclater, J. G. (1977). An analysis of the variation of ocean floor bathymetry
333 and heat flow with age. *Journal of Geophysical Research*, 82(5), 803–827.
- 334 Pebesma, E. (2004). Multivariable geostatistics in S: The gstat package. *Computers &*
335 *Geosciences*, 30, 683–691.
- 336 Pebesma, E. (2018). Simple Features for R: Standardized Support for Spatial Vector Data.
337 *The R Journal*, 10(1), 439–446. <https://doi.org/10.32614/RJ-2018-009>
- 338 Pollack, H. N., & Chapman, D. S. (1977). On the regional variation of heat flow, geotherms,
339 and lithospheric thickness. *Tectonophysics*, 38(3-4), 279–296.
- 340 Pollack, H. N., Hurter, S. J., & Johnson, J. R. (1993). Heat flow from the earth's inte-
341 rior: Analysis of the global data set. *Reviews of Geophysics*, 31(3), 267–280.
- 342 PROJ contributors. (2021). *PROJ coordinate transformation software library*. Open Source
343 Geospatial Foundation. Retrieved from <https://proj.org/>
- 344 Rudnick, R. L., McDonough, W. F., & O'Connell, R. J. (1998). Thermal structure, thick-
345 ness and composition of continental lithosphere. *Chemical Geology*, 145(3-4), 395–
346 411.
- 347 Sclater, J. G., & Francheteau, J. (1970). The implications of terrestrial heat flow obser-
348 vations on current tectonic and geochemical models of the crust and upper mantle
349 of the earth. *Geophysical Journal International*, 20(5), 509–542.
- 350 Scrucca, L. (2013). GA: A package for genetic algorithms in r. *Journal of Statistical Soft-*
351 *ware*, 53(4), 1–37.
- 352 Scrucca, L. (2016). On some extensions to GA package: Hybrid optimisation, parallelisi-
353 sation and islands evolution. *arXiv Preprint arXiv:1605.01931*.
- 354 Shapiro, N. M., & Ritzwoller, M. H. (2004). Inferring surface heat flux distributions guided
355 by a global seismic model: Particular application to antarctica. *Earth and Planetary
356 Science Letters*, 223(1-2), 213–224.
- 357 Stein, C. A., & Stein, S. (1992). A model for the global variation in oceanic depth and
358 heat flow with lithospheric age. *Nature*, 359(6391), 123–129.

- 359 Stein, C. A., & Stein, S. (1994). Constraints on hydrothermal heat flux through the oceanic
360 lithosphere from global heat flow. *Journal of Geophysical Research: Solid Earth*, 99(B2),
361 3081–3095.
- 362 Syracuse, E. M., & Abers, G. A. (2006). Global compilation of variations in slab depth
363 beneath arc volcanoes and implications. *Geochemistry, Geophysics, Geosystems*, 7(5).
- 364 Wada, I., & Wang, K. (2009). Common depth of slab-mantle decoupling: Reconciling
365 diversity and uniformity of subduction zones. *Geochemistry, Geophysics, Geosystems*,
366 10(10).
- 367 Wilkinson, M. D., Dumontier, M., Aalbersberg, Ij. J., Appleton, G., Axton, M., Baak,
368 A., et al. (2016). The FAIR guiding principles for scientific data management and
369 stewardship. *Scientific Data*, 3(1), 1–9.